NANO · MICRO small
www.small-journal.com

Controlling Nanoscale Thermal Expansion of Monolayer Transition Metal Dichalcogenides by Alloy Engineering

*Xuan Hu, Zahra Hemmat, Leily Majidi, John Cavin, Rohan Mishra, Amin Salehi-Khojin, Serdar Ogut, and Robert F. Klie**

2D materials, such as transition metal dichalcogenides (TMDs), graphene, and boron nitride, are seen as promising materials for future high power/high frequency electronics. However, the large difference in the thermal expansion coefficient (TEC) between many of these 2D materials could impose a serious challenge for the design of monolayer-material-based nanodevices. To address this challenge, alloy engineering of TMDs is used to tailor their TECs. Here, in situ heating experiments in a scanning transmission electron microscope are combined with electron energy-loss spectroscopy and first-principles modeling of monolayer $Mo_{1-x}W_xS_2$ with different alloying concentrations to determine the TEC. Significant changes in the TEC are seen as a function of chemical composition in $Mo_{1-x}W_xS_2$, with the smallest TEC being reported for a configuration with the highest entropy. This study provides key insights into understanding the nanoscale phenomena that control TEC values of 2D materials.

Low-dimensional materials, such as transition metal dichalcogenides (TMDs), have attracted considerable attention as promising materials for the next generation of electronic devices. Both monolayer and few-layer TMDs have been suggested as materials with a variety of unique properties,[1,2] including spin–orbit coupling effects for spintronic applications,[3,4] superconductivity,[1] ferromagnetism,[2] a direct bandgap in the optimal range for solar cell applications[5,6] and transistors.[7,8] Moreover, it was previously shown that the bandgap in 2H-TMDs can be tuned using selective doping, which allows them to have high on–off ratios[9] for low-power logic and switching applications.[10,11] When single or few-layer TMD materials are combined with graphene and hexagonal boron nitride (hBN) to form heterostructures, novel electronic properties have been discovered, including fluorescence intermittency,[3] high mobility, and optical transparency when integrated in thin film transistors,[12] fractional quantum Hall effects,[4] or valley-polarized excitons.[5] Moreover, tunneling-field effect transistors formed by stacking of these atomically thin 2D materials can enable energy-efficient transistors for digital and analog circuit applications.[13]

In this study, we report that the thermal expansion coefficient (TEC) of 2D TMDs can be engineered by changing the composition of alloyed 2D materials. In particular, we determine the TEC of $Mo_{1-x}W_xS_2$ ranging from MoS_2 to WS_2 using a combination of scanning transmission electron microscopy (STEM) and electron energy-loss spectroscopy (EELS) and first-principles density-functional-theory (DFT)-based modeling.[7] Our results reveal that the TEC depends on the composition and is lower for all $Mo_{1-x}W_xS_2$ alloys compared to MoS_2 and WS_2, with a minimum in the TEC for the $Mo_{0.5}W_{0.5}S_2$ structure.

$Mo_xW_{1-x}S_2$ structures were synthesized via chemical vapor transport (CVT) method using desired amounts of molybdenum (Mo), tungsten (W), and sulfur (S) powders in evacuated ampules based on the stoichiometric ratios (see more details in the Experimental Section). The obtained powders were then exfoliated in isopropyl alcohol (IPA) solution followed by centrifugation and drop casting on a holey-carbon film supported by a holey SiN film (Protochips thermal E-chips) for TEM measurements. Figure S1 in the Supporting Information shows the dynamic light scattering (DLS) measurement of $Mo_{0.7}W_{0.3}S_2$ solution using a NiComp ZLS 380 system at room temperature. We find that the average size of the exfoliated flakes is 175 nm. **Figure 1**A shows a high-angle annular dark-field (HAADF) image of a freestanding $Mo_{0.7}W_{0.3}S_2$ flake spanning the hole in the carbon film. Figure 1B–D shows an atomic-column resolved HAADF image of several $Mo_{1-x}W_xS_2$ flakes ($x = 0.3, 0.5, 0.7$) with 2H hexagonal structure ($P6_3/mmc$) along the [001] zone axis. Here, the transition metals (Mo or W) form a hexagonal lattice, while the S sublattice is not visible in the HAADF imaging mode. Moreover, the HAADF images

Dr. X. Hu, Prof. S. Ogut, Prof. R. F. Klie
Department of Physics
University of Illinois at Chicago
Chicago, IL 60607, USA
E-mail: rfklie@uic.edu
Z. Hemmat, L. Majidi, Prof. A. Salehi-Khojin
Department of Mechanical and Industrial Engineering
University of Illinois at Chicago
Chicago, IL 60607, USA
J. Cavin
Department of Physics
Washington University in St. Louis
St. Louis, MO 63130, USA
Prof. R. Mishra
Department of Mechanical Engineering and Materials Science and Institute of Materials Science and Engineering
Washington University in St. Louis
St. Louis, MO 63130, USA

DOI: 10.1002/smll.201905892

allow us to distinguish between the Mo and W atoms, since the image contrast is directly proportional to the atomic number, Z, and the heavier W atoms will appear as brighter spots in the images. Based on the comparison of these three samples, we find that the concentration of W atoms, i.e., x in $Mo_{1-x}W_xS_2$, increases as expected for $0.3 \leq x \leq 0.7$.

The positions of the Mo and W atoms are identified using 2D Gaussian fitting,[14] and the resulting positions are marked as red and blue circles in Figure 1B–D for W and Mo atoms, respectively. Based on the identified distributions, the alloying degrees of W and Mo were calculated to be 99.4–100.9% and 99.4–99.9% for different alloy concentrations, respectively (see more details in the Supporting Information and ref. [15]). This indicates that the high-contrast W atoms are homogeneously distributed into the MoS_2 structure at the atomic scale and there is no evidence of any local ordering or clustering of W and Mo atoms. The observed formation of stable $Mo_{1-x}W_xS_2$ alloys across the entire compositional range with disorder of Mo/W atoms is in excellent agreement with our DFT-based results of the alloy formation energies. We performed a cluster expansion-based search for ordered and disordered $Mo_{1-x}W_xS_2$ alloys for the entire composition range. We find that the mixing enthalpy (ΔH) of the disordered alloys at all compositions is negative as shown in Figure 1E, which explains the lack of phase segregation between MoS_2 and WS_2 in the STEM experiments. Moreover, we find 10 ordered alloys on the convex hull that are expected to be thermodynamically stable. The number of stable ordered alloys presented here is larger than that reported in a previous study, which had only considered symmetric structures at $x = 1/3$ and $2/3$.[16] However, due to the greater configurational entropy of the disordered alloys, we predict that chemically disordered $Mo_{1-x}W_xS_2$ alloys have lower free energy than ordered alloys for temperatures above 50 K (see the order–disorder phase diagram in the Supporting Information), which also explains the lack of any locally ordered structures in the synthesized samples.

X-ray photoelectron spectroscopy (XPS) was used to confirm the atomic composition of the alloyed structures. Figure 1C shows the Mo 3d, W 4f, and S 2p core levels for the $Mo_{0.7}W_{0.3}S_2$ sample. Our XPS results confirm the presence of MoS_2 and WS_2 phases corresponding to major peaks of Mo 3d at 229 and 232 eV as well as W 4f peaks at 34 and 35.5 eV. Our high-resolution XPS quantification analyses indicate the composition ratio of 69.2–30.8% for Mo:W. The XPS results on other synthesized materials (Section S2, Supporting Information) confirm the stoichiometry of the other $Mo_{1-x}W_xS_2$ alloys. Raman spectroscopy was also performed on synthesized $Mo_{1-x}W_xS_2$ samples with different compositions. Our results in Figure 1D show distinct peaks of MoS_2 at ≈382 and ≈408 cm^{-1} and WS_2 at ≈355 and ≈420 cm^{-1}. Moving from $x = 0$ to $x = 1$, the peak located at ≈408 cm^{-1} shifts to ≈420 cm^{-1}, while the MoS_2-like peak at ≈382 cm^{-1} moves toward lower frequencies with a decrease in

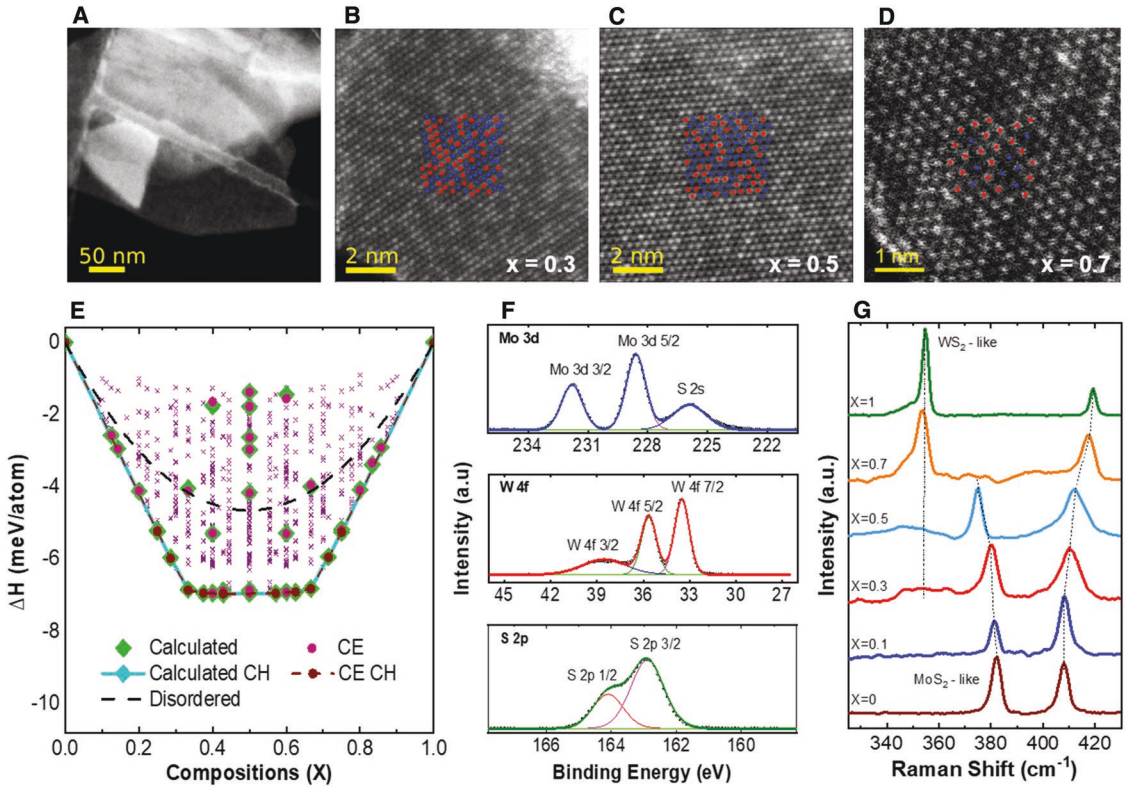

Figure 1. A) HAADF image of a $Mo_{0.3}W_{0.7}S_2$ flake suspending across the holes on the carbon films. B–D) Atomic-resolution HAADF images of $Mo_{1-x}W_xS_2$ ($x = 0.3$, 0.5, 0.7) at 423 K with identified atom locations marked in the centers (red and blue circles for W and Mo atoms, respectively). E) Convex hull plot of $Mo_{1-x}W_xS_2$ generated using the cluster expansion method. The circles and diamonds represent the calculated training set and corresponding predictions, respectively. The x's represent predictions without corresponding calculations. F) XPS results of synthesized $Mo_{0.3}W_{0.7}S_2$. G) Raman spectra of $Mo_{1-x}W_xS_2$ with different W compositions.

intensity. A new WS_2-like peak is observed at $x = 0.3$, which has an increase in intensity while shifting toward ≈355 cm^{-1} at $x = 1$.[17]

In situ heating experiments using a double-tilt Protochips Aduro stage were combined with ADF imaging and EELS to image the atomic structure and measure the shift of the plasmon peaks as a function of sample temperature. Each TEM sample was first gradually heated from room temperature to 723 K. To monitor the structural change during the heating process, atomic-resolution HAADF images were collected at several different sample temperatures, from 423 to 723 K in 100 K increments. The heating process was followed by a gradual lowering of the sample temperature while low-loss EEL spectra were collected at four sample temperatures between 723 and 423 K with $\Delta T = 100$ K. The energy scale for all EEL spectra was calibrated using the zero-loss peak, and the intensity was normalized with respect to a 40–60 eV energy loss window after the plasmon energy area (5–40 eV energy loss). The initial sample heating process was used to minimize the sample contamination with mobile carbon species, which will prevent the acquisition of the plasmon EELS. In addition, imaging was used to monitor any structural changes as the result of the in situ heating process, as discussed below.

Figure 2A shows the atomic-resolution HAADF images of $Mo_{1-x}W_xS_2$ at four sample temperatures (423–723 K). During the heating process, the monolayer area (indicated by yellow rectangle) gradually receded, which could be either due to the temperature-induced creation of vacancies or due to the strain induced by the mismatch in thermal expansion between the monolayer area and nearby few-layer region. As a result, additional atoms accumulated at the edge of two-layers area (indicated by the red rectangle), and triangle-shaped vacancy clusters that have been reported in the literature[18] are formed, which also extend into the two-layer thick regions of the sample (indicated by the blue arrow). In thicker area of the sample, the in situ heating results in the formation of vacancy cluster (seen as triangular shape) and clustering of atoms on the surfaces. However, the relative distribution of Mo and W atoms did not change significantly. It is important to note here that the creation of vacancies and surface atom clusters can influence the low-loss EEL spectra. Therefore, our EELS measurements are performed only in areas with minimum structural change to eliminate any effects of defects, atom clustering, and vacancies. Moreover, due to the high spatial resolution (i.e., 2.1 nm[19]) of our approach and the ability to perform simultaneous imaging, we can measure the thermal expansion coefficients via the plasmon peak shift from regions without visible defects. This is to ensure that our measurements do not induce additional defects at elevated temperatures.

As an example of our EELS measurements, Figure 2B shows an atomic-resolution HAADF image of a $Mo_{0.3}W_{0.7}S_2$ flake at $T = 723$ K and corresponding plasmon energy shift (Figure 2C) acquired from the area indicated by the red box in Figure 2B at different temperatures. In this monolayer sample, we do not detect any sign of defect formation during our measurements. The plasmon energy shift was measured to be −1.0 meV K^{-1},

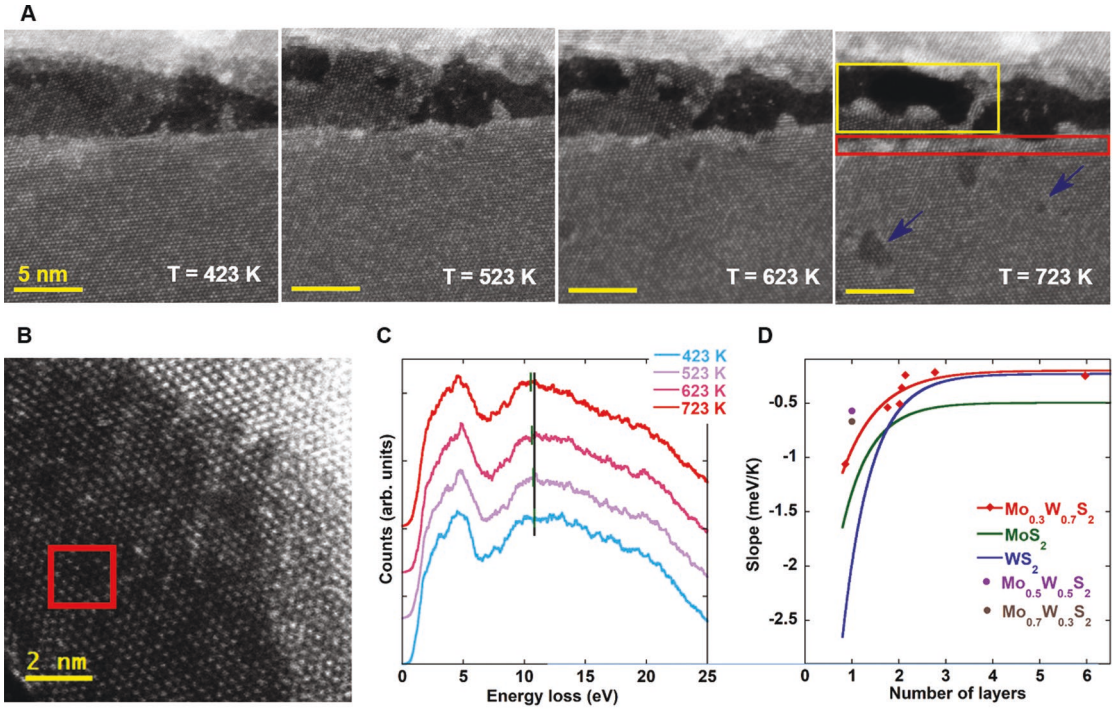

Figure 2. A) Atomic-resolution HAADF image of $Mo_{0.5}W_{0.5}S_2$ at different temperatures. The yellow and red boxes, as well as the blue arrows indicate the defects forming during the heating process. B) HAADF image of $Mo_{0.3}W_{0.7}S_2$ and C) the corresponding low-loss EELS recorded in the red rectangle area at different temperatures. The green lines present the plasmon peak positions by the Gaussian fitting. The black line indicating the plasmon peak at $T = 423$ K is used to provide a better visualization of the red shift during heating. D) The shift of the plasmon peak energy as a function of $Mo_{1-x}W_xS_2$ layers for $0.3 \leq x \leq 0.3$. The two endmembers are also plotted.

which is smaller than both pure MoS_2 (–1.5 meV K^{-1}) and WS_2 (–2.5 meV K^{-1}), we have reported previously.[19] Figure 2D shows a summary of the plasmon energy shifts for different sample compositions and number of layers. The results of alloyed $Mo_{1-x}W_xS_2$ are compared with pure MoS_2 and WS_2. We find that the measured plasmon peak shifts of the alloys are smaller than the range of values measured for MoS_2 and WS_2. This observation runs counter to the empirical Vegard's law, which is frequently followed by alloys, where a measured property of the alloy is a weighted average of the property of the end members.

To determine the thermal expansion coefficient for the three different types of alloyed samples, we performed first-principles modeling. To approximate the random distribution of Mo and W in the $Mo_{1-x}W_xS_2$ structures while using a periodic simulation frame (as required for our calculations), we utilized special quasirandom structures (SQS) using a Monte-Carlo algorithm implemented in the Alloy Theoretic Automated Toolkit (ATAT).[20,21] The SQS code considers the correlation of the nearby sites and creates a structure with correlations close enough to the one from the truly disordered structure. The SQS of monolayer $Mo_{1-x}W_xS_2$ (x = 0.33, 0.5, 0.67) were generated and relaxed to the corresponding energetically stable configuration. **Figure 3**A presents a typical SQS of monolayer $Mo_{0.33}W_{0.67}S_2$ in the top and side view. In addition to the SQS structures, we also determined the atomic configuration directly from the atomic-resolution ADF images and generated an ordered structure, where two types of atomic structures are alternatively stacked along the *b*-axis. A complete discussion of each structure is included in the Supporting Information. We find a very close match between the experimental and simulated alloy atomic structures.

Based on these relaxed SQS, the frequency dependent dielectric functions ($\varepsilon(\omega)$) for monolayer $Mo_{1-x}W_xS_2$ (x = 0.33, 0.5, 0.67) are then calculated using the random phase approximation (RPA). We selected a monolayer structure for $Mo_{1-x}W_xS_2$ with x = 0.33 (0.67) as an approximation to the structure we measured experimentally with x = 0.3 (0.7). The calculated low-loss EELS signals, specifically $\mathrm{Im}(-1/\varepsilon)$, are simulated to determine the plasmon energy shift (γ_a) as a function of lattice expansion. For more details, see our previous publication detailing the methodology used here.[19] The calculated plasmon energy shift γ_a as a function of x for monolayer $Mo_{1-x}W_xS_2$ is plotted in Figure 3B. It can be clearly seen that γ_a reaches a maximum value for a 50% alloying concentration (i.e., $Mo_{0.5}W_{0.5}S_2$). Based on this simulated shift (γ_a) and the experimental plasmon shift (R), the thermal expansion coefficients for monolayer $Mo_{1-x}W_xS_2$ alloys were determined using $-R/\gamma_a$, where α is the thermal expansion coefficient. The measured values for α as a function of x are shown in Figure 3B and displayed as a full list in **Table 1**. It is interesting to note that the thermal expansion coefficient does not show a linear relationship with the alloy concentration, x. In fact, the thermal expansion coefficients are lower for all $Mo_{1-x}W_xS_2$ alloys and reach a minimum value of 3.51×10^{-5} K^{-1} for $Mo_{0.5}W_{0.5}S_2$.

The random distribution of Mo and W atoms alters the nearest neighbor surroundings around any given atom and leads to different metal–sulfur bond distances that range from 2.41–2.43 Å (3.18–3.20 Å between transition metals) as observed in the optimized SQS structure of $Mo_{0.5}W_{0.5}S_2$ (see Section S8

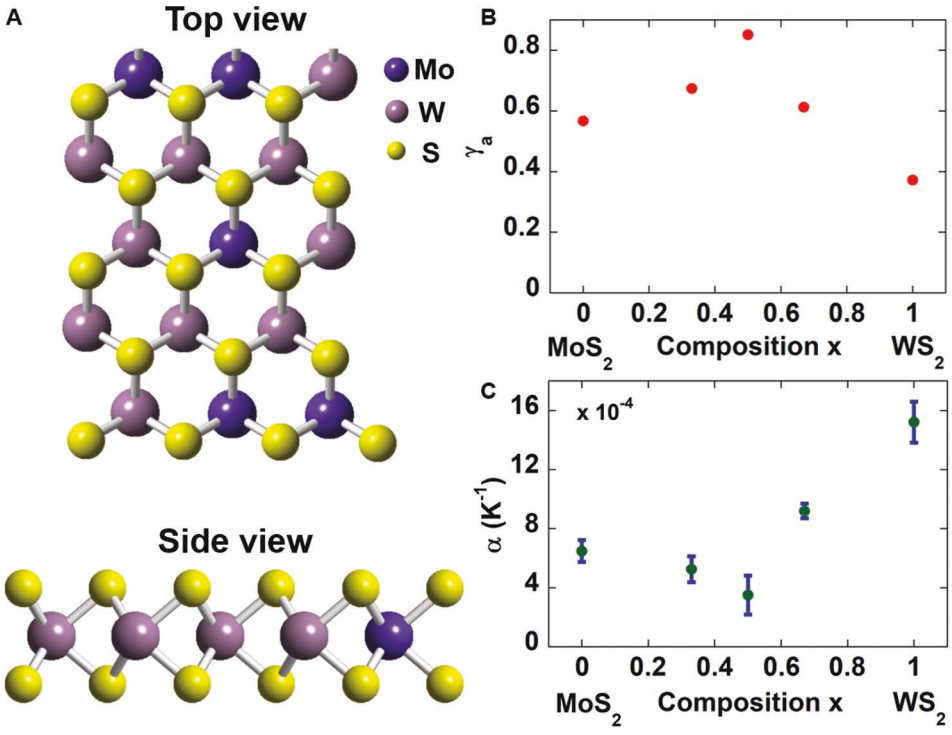

Figure 3. A) The special quasirandom structure (SQS) of $Mo_{0.33}W_{0.67}S_2$ in the top and side view. B) Simulate shift as a function lattice expansion and C) the thermal expansion coefficients (α) of monolayer $Mo_{1-x}W_xS_2$ at different alloying concentrations (x = 0,[22] 0.3, 0.5, 0.7, 1[22]).

Table 1. The measured in-plane thermal expansion coefficient (10^{-5} K^{-1}) of monolayer $Mo_{1-x}W_xS_2$ at different alloying concentrations.

System	$x = 0$	$x = 0.3$	$x = 0.5$	$x = 0.7$	$x = 1$
TEC	6.59 ± 0.75[a)]	5.25 ± 0.88	3.51 ± 1.32	9.20 ± 0.50	15.21 ± 1.38[a)]

[a)]The data of pure materials ($x = 0$ or 1) are from ref. [22].

in the Supporting Information for more details about the distortions). One possibility is that the measured decrease in the thermal expansion coefficient for $Mo_{1-x}W_xS_2$ alloys could be due to these local distortions, but we find that the freezing of local distortions leads to only small changes in γ. A more direct, but computationally demanding, approach to understand how alloying and local distortions could affect thermal expansion is to obtain TECs directly from first principles through the calculation of the phonon band structure and the mode Grüneisen parameters.[23] Work along this line is ongoing and will be presented elsewhere. We also conjecture that ordering of atoms, for example, by creating superlattice of MoS_2 and WS_2 in monolayer forms[24] will provide an additional level of control over the thermal expansion coefficient.

In summary, we utilized our in situ STEM/EELS nanoscale technique to measure the thermal expansion coefficients of monolayer $Mo_{1-x}W_xS_2$ with $0.3 \leq x \leq 0.7$. We found that during the heating process, the crystal structures can change dramatically due to the formation and diffusion of defects. Atomic-resolution imaging was used to monitor this change and provide a guide for our EELS measurements and to eliminate the effects of defects on the low-loss plasmon peak study. Combining the experimental temperature dependent plasmon peak shift with the simulated lattice-expansion dependent EELS signal, the thermal expansion coefficients of monolayer $Mo_{1-x}W_xS_2$ were determined. We found that the TECs are reduced compared to pure MoS_2 and WS_2 as the result of alloying and reaches a minimum for structure showing the highest entropy, $Mo_{0.5}W_{0.5}S_2$. This reported reduction in the thermal expansion coefficient as a function of alloy concentration demonstrates the potential to control the thermal expansion coefficient in 2D materials and to engineer the thermal expansion mismatch between different 2D materials. More interestingly, at heterointerfaces, where the alloying concentration does not abruptly change, the nonlinear effect reported here may be of critical interest in the device design. Future studies of nanoscale thermal properties across the monolayer TMD in-plane heterostructures will be of great interest.

Experimental Section

Experimental Methods: $Mo_xW_{1-x}S_2$ structures were synthesized using desired amounts of molybdenum (Mo), tungsten (W), and sulfur (S) powders in evacuated ampules based on the stoichiometric ratios. The ampules were heated up in a two-zone furnace under vacuum to 1353 K for 21 h. The cold zone of the furnace was slowly cooled down to 1209 K over 71 h while the temperature of hot zone remained at 1353 K. The furnace was then cooled down to room temperature over 21 h. Through liquid-phase exfoliation technique, the obtained powders were exfoliated in IPA solution to prepare nanoflakes. The 300 mg of alloyed material powder was dispersed in 60 mL IPA (Sigma Aldrich, UHP) and exfoliated for 30 h. The solution was then centrifuged for 1 h. The top two third of the solution was extracted to obtain the final solution for the characterizations and TEM experiments.

Following solution preparation, the dispersed nanoflakes were drop cast on holey carbon films supported on Protochips thermal E-chips and dried for 5 min under an infrared. The grids were then annealed in vacuum under argon at 373 K for 4 h to remove any solvent residues. The samples were then kept in a vacuum desiccator until loaded into the microscope.

The TEM samples were characterized using an aberration-corrected JEOL JEM-ARM200CF equipped with a cold FEG and a Gatan Continuum EEL spectrometer, providing a sub-Å probe-size and 350 meV energy resolution. To control beam-induced damages during imaging and EELS acquisition, an 80 kV accelerating voltage with a 15 µA emission current was used. A 28 mrad convergence semiangle was selected for STEM and EELS. The HAADF images were recorded with detector angles ranging from 68 to 280 mrad. The EEL spectra were acquired with a dispersion of 0.05 eV per channel in the low-loss area.

For each in situ heating experiment, the sample was initially heated to 723 K and then the temperature was lowered by 100 K each time to record the data until 373 K was reached. At each sampled temperature, the sample was allowed to stabilize for half an hour (1 h for 723 K) or until no obvious drift was observed before the data acquisition.

Details about the Gaussian fitting of the bulk plasmon peaks were previously reported in ref. [19]. It is important to note here that the energy position of any peak in the electron energy-loss spectrum can be determined with a precision in excess of the energy-resolution of the EEL spectra using the types of curve fitting described in ref. [19].

Computational Methods: The energy dependence of the inelastic scattering was proportional to the energy-loss function, $\mathrm{Im}[-1/\varepsilon(q,E)]$. To simulate the low-loss EELS signals, the frequency dependent dielectric functions were calculated using the Vienna Ab initio Simulation Package (VASP), including local field effects in the RPA. For a sufficiently accurate simulation, a plane wave cutoff of 600 eV was chosen. For the smearing method, the tetrahedron method with Blochl corrections was used. Monkhorst-Pack *k*-point meshes were chosen as $21 \times 21 \times 1$. The vacuum in the out-of-plane direction was set as 30 Å. In order to have a sufficient description of the unoccupied states, the total number of bands was selected as double the number of occupied bands.

Supporting Information

Supporting Information is available from the Wiley Online Library or from the author.

Acknowledgements

X.H., Z.H., L.M., A.S.-K., and R.F.K. were supported by the National Science Foundation (EFRI 2-DARE EFMA-1542864 and DMREF CBET-1729420). S.O. was supported by the National Science Foundation's DMR-Ceramics program (DMR-1831406). J.C. and R.M. acknowledge support through NSF DMREF-1729787. The acquisition of UIC JEOL JEM ARM200CF was supported by an MRI-R2 grant from the National Science Foundation (Grant No. DMR-0959470) and the upgraded Gatan Continuum spectrometer was supported by a grant from the NSF (DMR-1626065). This work made use of instruments in the Electron Microscopy Service and the High Performance Computing Clusters at Research Resources Center, UIC. This work used resources of the National Energy Research Scientific Computing Center, a DOE Office of Science User Facility supported by the Office of Science of the U.S. Department of Energy under Contract No. DE-AC02-05CH11231, and of the Extreme Science and Engineering Discovery Environment (XSEDE), which is supported by NSF grant number ACI-1548562.

Conflict of Interest

The authors declare no conflict of interest.

Keywords

alloys, electron energy-loss spectroscopy, scanning transmission electron microscopy, thermal expansion coefficient, transition metal dichalcogenides

Received: October 14, 2019
Revised: November 19, 2019
Published online: December 12, 2019

[1] Q. H. Wang, K. Kalantar-Zadeh, A. Kis, J. N. Coleman, M. S. Strano, *Nat. Nanotechnol.* **2012**, *7*, 699.
[2] W. Choi, N. Choudhary, G. H. Han, J. Park, D. Akinwande, Y. H. Lee, *Mater. Today* **2017**, *20*, 116.
[3] D. Xiao, G. Liu, W. Feng, X. Xu, W. Yao, *Phys. Rev. Lett.* **2012**, *108*, 196802.
[4] B. Yang, M. Tu, J. Kim, Y. Wu, H. Wang, J. Alicea, R. Wu, M. Bockrath, J. Shi, *2D Mater.* **2016**, *3*, 031012.
[5] E. Singh, K. S. Kim, G. Y. Yeom, H. S. Nalwa, *RSC Adv.* **2017**, *7*, 28234.
[6] M. Bernardi, M. Palummo, J. C. Grossman, *Nano Lett.* **2013**, *13*, 3664.
[7] B. Radisavljevic, A. Radenovic, J. Brivio, V. Giacometti, A. Kis, *Nat. Nanotechnol.* **2011**, *6*, 147.
[8] M. Chhowalla, D. Jena, H. Zhang, *Nat. Rev. Mater.* **2016**, *1*, 16052.
[9] C. J. Shih, Q. H. Wang, Y. Son, Z. Jin, D. Blankschtein, M. S. Strano, *ACS Nano* **2014**, *8*, 5790.
[10] S. Kim, A. Konar, W. S. Hwang, J. H. Lee, J. Lee, J. Yang, C. Jung, H. Kim, J. B. Yoo, J. Y. Choi, Y. W. Jin, S. Y. Lee, D. Jena, W. Choi, K. Kim, *Nat. Commun.* **2012**, *3*, 1011.
[11] J. Gusakova, X. Wang, L. L. Shiau, A. Krivosheeva, V. Shaposhnikov, V. Borisenko, V. Gusakov, B. K. Tay, *Phys. Status Solidi A* **2017**, *214*, 1700218.
[12] S. Das, R. Gulotty, A. V. Sumant, A. Roelofs, *Nano Lett.* **2014**, *14*, 2861.
[13] A. M. Ionescu, H. Riel, *Nature* **2011**, *479*, 329.
[14] M. Nord, P. E. Vullum, I. MacLaren, T. Tybell, R. Holmestad, *Adv. Struct. Chem. Imaging* **2017**, *3*, 9.
[15] D. O. Dumcenco, H. Kobayashi, Z. Liu, Y. S. Huang, K. Suenaga, *Nat. Commun.* **2013**, *4*, 1351.
[16] W. Tan, Z. Wei, X. Liu, J. Liu, X. Fang, D. Fang, X. Wang, D. Wang, J. Tang, X. Fan, *Sci. Rep.* **2017**, *7*, 15124.
[17] X. Zhang, X. F. Qiao, W. Shi, J. Bin Wu, D. S. Jiang, P. H. Tan, *Chem. Soc. Rev.* **2015**, *44*, 2757.
[18] W. Zhou, X. Zou, S. Najmaei, Z. Liu, Y. Shi, J. Kong, J. Lou, P. M. Ajayan, B. I. Yakobson, J. C. Idrobo, *Nano Lett.* **2013**, *13*, 2615.
[19] X. Hu, P. Yasaei, J. Jokisaari, S. Öğüt, A. Salehi-Khojin, R. F. Klie, *Phys. Rev. Lett.* **2018**, *120*, 05590.
[20] A. Van De Walle, P. Tiwary, M. De Jong, D. L. Olmsted, M. Asta, A. Dick, D. Shin, Y. Wang, L. Q. Chen, Z. K. Liu, *Calphad* **2013**, *42*, 13.
[21] J. Kang, S. Tongay, J. Li, J. Wu, *J. Appl. Phys.* **2013**, *113*, 143703.
[22] Q. Cai, D. Scullion, W. Gan, A. Falin, S. Zhang, K. Watanabe, T. Taniguchi, Y. Chen, E. J. G. Santos, L. H. Li, *Sci. Adv.* **2019**, *5*, eaav0129.
[23] P. Pavone, K. Karch, O. Schutt, D. Strauch, W. Windl, P. Giannozzi, S. Baroni, *Phys. Rev. B* **1993**, *48*, 3156.
[24] S. Xie, L. Tu, Y. Han, L. Huang, K. Kang, K. U. Lao, P. Poddar, C. Park, D. A. Muller, R. A. DiStasio, J. Park, *Science* **2018**, *359*, 1131.

